Journal of Power Sources 184 (2008) 191–196

Contents lists available at ScienceDirect

Journal of Power Sources

journal homepage: www.elsevier.com/locate/jpowsour

Ink-jet printing of electrolyte and anode functional layer for solid oxide fuel cells

D. Young[a], A.M. Sukeshini[a,*], R. Cummins[a], H. Xiao[b], M. Rottmayer[c], T. Reitz[c]

[a] Department of Mechanical and Materials Engineering, Wright State University, 3640 Colonel Glenn Highway, Dayton, OH 45430, United States
[b] Aerospace Power and Propulsion, UES Corp., Dayton, OH 45432, United States
[c] The Air Force Research Laboratory, Propulsion Directorate, 1950 Fifth Street, Building 18, Wright-Patterson Air Force Base, OH 45433, United States

ARTICLE INFO

Article history:
Received 10 April 2008
Received in revised form 3 June 2008
Accepted 4 June 2008
Available online 18 June 2008

Keywords:
Ink-jet printing
SOFC
Anode functional layer
YSZ electrolyte
Microstructure

ABSTRACT

In this work, solid oxide fuel cells were fabricated by ink-jet printing. The cells were characterized in order to study the resulting microstructure and electrochemical performance. Scanning electron microscopy revealed a highly conformal 6–12 μm thick dense yttria-stabilized zirconia electrolyte layer, and a porous anode-interlayer. Open circuit voltages ranged from 0.95 to 1.06 V, and a maximum power density of 0.175 W cm^{-2} was achieved at 750 °C. These results suggest that the ink-jet printing technique may be used to fabricate stable SOFC structures that are comparable to those fabricated by more conventional ceramics processing methods. This study also highlights the significance of overall cell microstructural impact on cell performance and stability.

1. Introduction

Recently, there has been a concerted effort in the development of solid oxide fuel cells (SOFCs) owing to their potential for clean and efficient power generation [1,2]. New anode, cathode and electrolyte materials are being explored to improve SOFC performance, increase stability, and reduce operating temperatures [3–5]. Fundamental studies of basic transport mechanisms and interfacial gradation effects are being performed in order to reduce impedances and improve performance [6,7]. From a more applied perspective, stack configuration [8–10] and interconnect technologies [11] are being developed in order to facilitate the development of larger SOFC systems. In many of these areas, SOFC fabrication methods are generally considered to be limiting factors considering the need for automation and scalability [12]. Some SOFC structures are produced using traditional ceramic preparation methods such as powder pressing, tape casting, screen-printing, or conventional spray methods [13]. Other, more sophisticated methods, such as plasma spraying [14,15], vacuum deposition [16], and extrusion-based direct-write methods [17] are also reported.

Ink-jet printing has already been demonstrated as a method to fabricate various ceramic layers [18,19] and three-dimensional structures [20,21]. The extension of this work to SOFCs is a promising route to investigate. This technique is also being applied to polymer electrolyte fuel cell materials [22]. There are many attractive features to the ink-jetting process that suggest that it may be a desirable fabrication method. Ink-jet systems have relatively fine resolution control and typically produce droplets approximately 50 μm in diameter. Thus, ink-jet printing has the necessary deposition control to produce the layers needed for SOFCs, and most likely can also print the fine features required for optimized interconnect and metallization patterns. Ink-jetting has also been utilized as a method to fabricate functionally graded ceramic materials [23]. Finally, ink-jet printers range from lab-scale models that allow experimentation with customized inks, up to mass manufacturing systems that can print rapidly, and competitively, with other printing methods on an industrial scale. Investigations into the ink-jet printing of SOFC structures are relatively easy and accessible to researchers, but are also especially attractive since scale-up issues are mitigated by technological maturity.

In order to explore the applicability of ink-jet printing to SOFC materials and structures, a traditional set of SOFC electrolyte, anode and cathode materials were selected (Yttria-stabilized zirconia, nickel oxide and $La_{0.8}Sr_{0.2}MnO_3$, respectively). Selection of these conventional materials facilitates direct comparison to similar SOFCs that have been fabricated by other methods and previously reported. The electrolyte and anode-interlayer portions of the SOFC were prepared via ink-jet printing. The anode-support,

* Corresponding author. Tel.: +1 937 255 6227; fax: +1 937 656 7529.
E-mail address: mary.ayyadurai.ctr@wpafb.af.mil (A.M. Sukeshini).

0378-7753/$ – see front matter © 2008 Elsevier B.V. All rights reserved.
doi:10.1016/j.jpowsour.2008.06.018

Table 1
Ink formulation used for printing anode functional layer and electrolyte layer

Constituent	Anode interlayer (g)	Electrolyte (g)
α-Terpineol	10	10
YSZ	0.3	0.6
NiO	0.3	0
PAG	0.01	0.01
BBP	0.01	0.01
PVB	0.01	0.01

cathode layer and current collector structures were produced by more conventional means. This strategy was employed in order to isolate the effect of ink-jet printing to a sub-set of the SOFC structure, and allow a clearer determination of the potential effects of the ink-jet printing process on materials morphology and cell performance. The objective of this study was to explore the application of ink-jet deposition for production of thin layer SOFCs. The impact of this preparation methodology on cell morphology and performance are examined.

2. Experimental

2.1. Ink preparation and printing

In order to prepare suitable electrolyte and anode-interlayer inks, commercial sources of ceramic materials were selected. Yttria-stabilized zirconia (YSZ, 8 mol%, Tosoh, TZ-8YS) was used for both electrolyte and anode interlayer inks, and two nickel oxide powders (NiO, 20–30 nm diameter nanopowder, and NiO, 0.2–0.4 μm, Nextech) were used in the anode interlayer ink. α-Terpineol was selected as the ink carrier. In addition, a combination of polyvinyl butyral, butyl benzyl phthalate, and polyalkalyne glycol were utilized as binder and plasticizer constituents. All inks were prepared by simultaneous addition of powders, binder and plasticizers to α-terpineol, followed by >12 h of ball milling with 5 mm diameter YSZ beads in a glass container. The composition of solids used in the ink for the electrolyte and anode functional layer is shown in Table 1.

A DIMATIX DMP 2831 ink-jet printer was utilized for all experiments presented in this paper. Model 11610 cartridges were used, which have a linear array of 16 jets and deposit nominal 10 picoliter droplets of ink. This system also allows temperature control of the ink reservoir and jet pathways between room temperature and 60 °C. In order to improve the drying rates, a modified platen system was used which allowed expanded temperature ranges to be explored.

A conventional SOFC cell consists of five separate layers which include anode current collection, anode functional layer, electrolyte, cathode functional layer, and cathode current collection. For the anode interlayer approximately 1.5 mL of interlayer ink was injected into a DIMATIX cartridge. The cartridge was then loaded into the printer and the material was deposited onto a prepared substrate using an optimized jetting profile established for use with each ink. Anode functional layers were deposited using a series of 32 V, 2.944 μs pulses which resulted in stable jetting at a frequency of 3 kHz. The internal cartridge temperature was set to 58 °C in order to compensate for the relatively high viscosity of the terpineol carrier. The printer deposited the droplets in a square raster pattern, with a 15 μm separation between each neighboring droplet. This substantial droplet overlap was utilized to produce a smooth, homogeneous layer with minimal pinhole generation. Subsequent layers were added on top of the previous layer. As discussed previously, increased drying rates were facilitated by modification of the DIMATIX printer platen with a thick-film heater (Omega, EFH-15001) which was mounted on an insulating plate. A substrate temperature of 80 °C was observed to remove the α-terpineol at a sufficient rate such that the anode did not become saturated with liquid. Typically, multiple layers of the anode interlayer were deposited onto the substrate, followed by bisque firing at 950 °C. The electrolyte ink was then printed in a similar manner using different jetting parameters (31 V, 2.944 μs pulse at a frequency of 3 kHz).

2.2. Cell fabrication and electrochemical measurements

Two ink-jet printed SOFC cells, Cell-1 and Cell-2 were fabricated. The current voltage characteristics of these two cells are detailed in Section 3. Performance issues that were evident in Cell-1 motivated several changes in the fabrication sequence of Cell-2. While the primary objective was to change the particle size of NiO relative to YSZ in the anode functional layer in the second cell (Cell-2), many additional changes were made in this preliminary stage of development of printed cells, with a view toward obtaining satisfactory current voltage characteristics for a successful demonstration of printed SOFCs. Cell-1 was prepared with an anode interlayer ink containing NiO nanopowder (20–30 nm size) and YSZ (0.4 μm size). A total of 10 layers of the anode interlayer were printed onto a commercial anode support that consisted of isostatically laminated green tape NiO/YSZ (60/40 wt%, NewTech.) that was bisque fired at 950 °C. Over the printed interlayer, 20 layers of the electrolyte were printed. The anode/anode interlayer/electrolyte structure was then co-fired at 1375 °C for 2 h. A cathode functional layer with 50/50 wt% of LSM (strontium doped lanthanum manganate, $La_{0.8}Sr_{0.2}MnO_3$)/YSZ was prepared by ball milling the LSM and YSZ powders, solvents, plasticizer, and dispersant into a highly viscous ink for several hours and then hand painted over the electrolyte. The coupon was then sintered at 1200 °C for 1 h. Finally, a cathode layer was hand painted using LSM in an ink vehicle (LSM paste, NexTech) and sintered at 1200 °C. The diameter of the cathode functional layer and cathode was 13 mm. The cathode area was considered as active area for the cell and used as the basis for calculation of current density. Cell-2 was fabricated in a modified fashion. The support substrate for this cell was prepared using a powder mixture of NiO (20–30 nm)/YSZ with a 60/40 weight ratio. The mixture was ground in an agate mortar, uniaxially pressed into wafers and bisque fired at 950 °C. Ink preparation, printing procedures, and resulting layer thicknesses were all analogous to those discussed for the previous sample. The same electrolyte ink was used, but the anode interlayer ink was prepared using a NiO powder (0.2–0.4 μm) with an effective surface area (6.7 $m^2 g^{-1}$) designed to be close to that of the YZS starting material (≈6.1 $m^2 g^{-1}$). One extra bisque firing step was also introduced after the printing of the anode interlayer. The sintering temperature of the anode/anode interlayer/electrolyte for this cell was 1400 °C. The cathode functional layer and cathode layer for Cell-2 were prepared in a manner similar to Cell-1. The differences between Cell-1 and Cell-2 are tabulated in Table 2.

Table 2
Differences in starting materials and processing method for Cell-1 and Cell-2

Materials/process	Cell-1	Cell-2
Anode interlayer ink particle size		
YSZ	0.4 μm	0.4 μm
NiO	20–30 nm	0.2–0.4 μm
Anode support	Tape cast	Die-pressed
Particle size in support		
NiO in NiO/YSZ	–	20–30 nm
Interlayer bisque	No	Yes, 950 °C
Sintering temperature of anode/anode interlayer/electrolyte	1375 °C	1400 °C

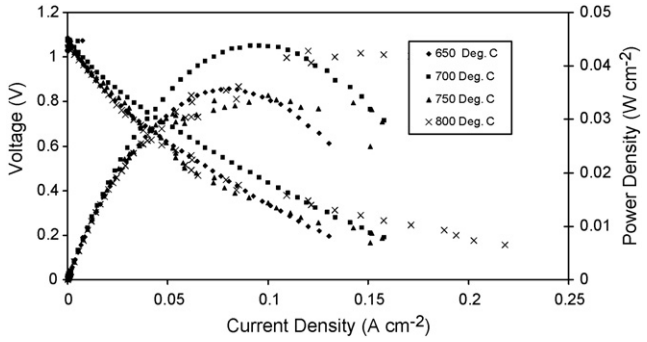

Fig. 1. Performance curve for Cell-1 in the temperature range from 650 to 800 °C.

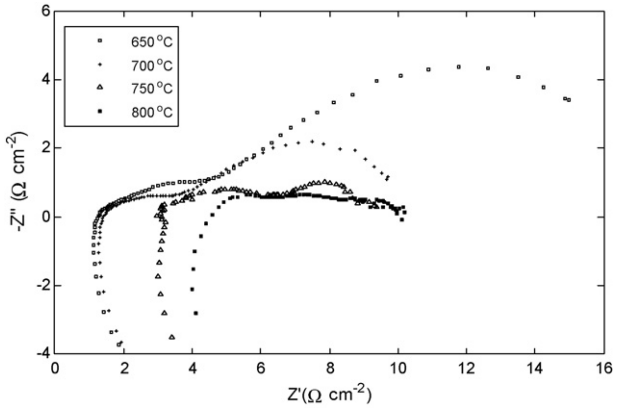

Fig. 2. Impedance plot at open circuit for Cell-1 at different temperatures.

Silver leads were attached on the cathode and anode sides using gold paste. The cells were then glued onto one end of a ceramic tube using a ceramic paste (Ultratemp 516) and housed in a tube furnace. During characterization of each cell, the furnace was slowly heated to desired temperatures (up to 800 °C) for electrochemical characterization. The anode side was reduced in forming gas (5% hydrogen in argon), while the cathode side was exposed to forced air. After reducing for 1–2 h, the anode side was exposed to dry hydrogen at a flow rate of 65 sccm.

The cell performance and electrochemical impedance spectra were measured using a multi-channel electrochemical test station comprised of a Solartron 1470E potentiostat/galvanostat combined with a Solartron 1450 frequency response analyzer. Impedance spectroscopy measurements were made in potentiostatic mode, under open circuit conditions, over a frequency range of 1 MHz to 50 mHz. For the impedance measurements, the excitation amplitude remained fixed at 10 mV. After electrochemical testing, the cells were cooled to room temperature with the anode side exposed to a reducing atmosphere of forming gas. After cooling, the morphology and microstructure were characterized using a JEOL JSM7401-F field-emission scanning electron microscope.

3. Results and discussion

3.1. Ink viscosity and shelf life

The viscosity of inks used was characterized with a laboratory-grade manual viscometer at room temperature and at 47 °C. The viscosities of pure terpineol and the YSZ ink used in this study were measured to be 70 and 73 cps at room temperature, respectively. At 47 °C, the viscosity values were observed to be 6.2 and 6.5 cps, respectively. The viscosity of these inks is similar to that of pure terpineol, at both low and high temperatures. This is consistent with the low solids loading utilized in this work (<5 vol.%).

In addition, the inks prepared for this study retained a visually stable suspension for periods longer than 4 weeks. A more convincing observation, suggesting stable suspension properties, was that ink-jet cartridges containing these inks were observed to produce stable jets for longer than 4 weeks. This can only occur if the oxide particles remain in suspension, since particle settling will quickly clog the internal fluidic pathways of the ink-jet assembly.

3.2. Current–voltage and impedance of printed cells

Fig. 1 shows the *V–I* curve of Cell-1. Open circuit voltages (OCV) were observed to range from 1.07 to 1.13 V, depending on the temperature. As temperature increased from 650 to 700 °C, the current density and power density are seen to increase. However, at 750 °C both current and power density exhibited a decrease and this trend continues at 800 °C. The current and power curves at 800 °C show instability between 0.67 and 0.38 V. When the overpotential is further increased, the slope of the *V–I* curve is seen to decrease to values lower than those exhibited at other temperatures. Fig. 2 shows the impedance plot, under open circuit conditions, for Cell-1 in the temperature range from 650 to 800 °C. Each impedance plot appears to be a superposition of several arcs, each with a characteristic ω_{max}. This superposition of arcs is more readily seen for the impedance spectrum at 650 °C. Each arc is generally interpreted to represent a single process within the SOFC. These processes may be physical or electrochemical, and can take place in the bulk of the electrodes or electrolyte, or at the electrolyte/electrode interfaces. Typically, processes such as ionic conductivity in electrolyte and charge transfer reactions at electrode/electrolyte interfaces occur at higher frequencies while processes such as diffusion and adsorption occur at lower frequencies. While simple impedance arcs can be modeled quite effectively using equivalent circuits consisting of RC combinations [24], more complex polarization mechanisms that result in situations where several arcs are superposed can be modeled using a distribution of relaxation times to meaningfully extract details of the various individual processes involved [25]. Nevertheless, important broad diagnostic information can be obtained from impedances even in the absence of detailed modeling. Trends seen in Fig. 2 corroborate the results seen in the *V–I* curve (Fig. 1). The serial resistance, R_Ω (intercept on the real axis at high frequency), shows a marginal decrease as the temperature is raised from 650 to 700 °C and for further increase in temperature, R_Ω increases appreciably. The polarization resistance R_p (the difference in intercept between low and high frequency) decreases with increase in temperature up to 750 °C and does not change significantly with further increase in temperature to 800 °C. The interplay of R_Ω and R_p dictate the slopes in the *V–I* curve of Fig. 1. The observed trend of increasing R_Ω and decreasing R_p with increase in temperature might be suggestive of improving cathode performance as the temperature increases and a deteriorating anode, or anode/electrolyte interface due to microstructural changes. However, de-lamination can be ruled out due to the fact that R_p does not increase proportionally with R_Ω. The currently seen trend is more likely indicative of a loss in surface area at the anode interlayer/electrolyte and or anode interlayer/anode interfaces. An unfavorable microstructure might lead to this sort of anode and/or anode interlayer failure. This may be due to several factors, typically sintering temperature, particle size mismatch, etc., influencing the anode's and/or anode interlayer's sinterability and the resulting microstructure.

Fig. 3 shows the performance curve for Cell-2 in the temperature range from 650 to 800 °C. Open circuit voltages were dependent on temperature and ranged from 0.99 to 1.07 V. A current density

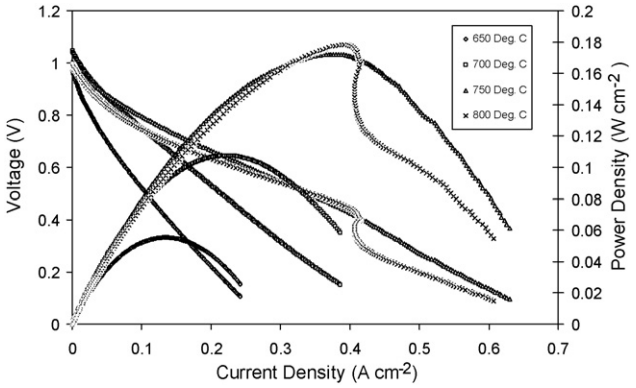

Fig. 3. Performance curve for Cell-2 in the temperature range from 650 to 800 °C.

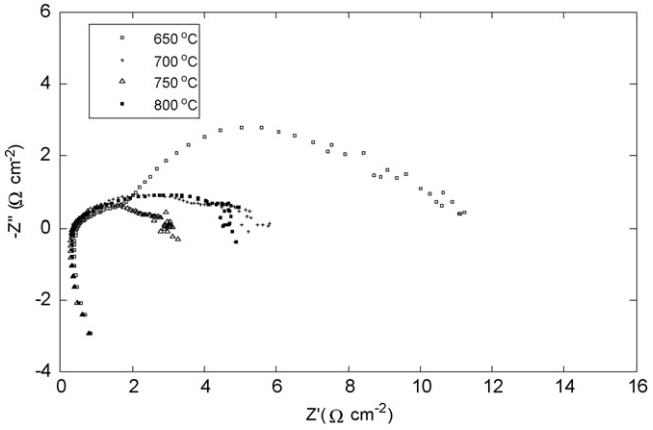

Fig. 4. Impedance plot at open circuit for Cell-2 at different temperatures.

close to 500 mA cm^{-2} was obtained at 300 mV at 750 °C. A maximum power density of 0.175 W cm^{-2} was achieved at 750 °C. The current density and maximum power density of Cell-2 are seen to increase with increasing temperatures. However some electrochemical instability can be seen was observed at 800 °C, with the appearance of a redox-like process around 0.45 V. It can be seen that the overall performance of Cell-2 is much higher than that of Cell-1, in terms of current and power density. The overall improvement in the current value of Cell-2 relative to Cell-1 is likely due to an improved overall cell microstructure determined by one or more factors associated with choice of precursor materials and/or processing. For example, the nano-sized NiO in the anode, with its larger surface area could have contributed to an additional triple phase boundary at the interface for electrochemical reactions and hence higher current values. Fig. 4 shows the impedance plot at open circuit at different temperatures, from 650 to 800 °C. On comparing Fig. 4 with Fig. 2, it is immediately clear that the normalized impedances of Cell-2 are much lower than those of Cell-1 at all temperatures. Both the serial resistance R_Ω and the polarization resistance R_p have decreased. The serial resistance appears to be almost unaffected by temperature. This may suggest large contact resistances and other ohmic resistances contributing to R_Ω in addition to the electrolyte resistance. The polarization resistance decreases with increasing temperature up to 750 °C. However at 800 °C, R_p is observed to increase. This feature seems to correlate to the instability observed at 800 °C. The behavior observed at 800 °C could possibly be due to microstructural changes in the anode or anode/electrolyte interface, owing to the large difference in particle size of YSZ compared with NiO in the anode support.

3.3. Microstructural assessment

Fig. 5a and b shows the fracture cross-sectional scanning electron micrograph of Cell-1 and Cell-2, respectively after electrochemical testing. The electrolytes of both cells are dense with very few blind holes. The electrolyte of Cell-2 is about 6 μm in thickness (lower marker in figure). An anode interlayer (lower marker in figure) of roughly the same thickness as the electrolyte can also be observed. The electrolyte for Cell-1 is nearly twice (~12 μm) as thick of Cell-2 with an interlayer as thick as the electrolyte. Besides a slight difference in porosity of the interlayers, with the interlayer of Cell-1 being somewhat less porous than that of Cell-2, no distinct difference can be seen. A distinct difference can be seen in the anode microstructures of the two cells. The anode of Cell-1 has uniform porosity while that of Cell-2 has non-uniform pores and larger agglomerated particles of the composite phase. Part of a porous cathode for Cell-1 and complete cathode for cell-2 can be seen. Fig. 6 shows the micrographs of the cells at a lower magnification to highlight the anode microstructure. Agglomerates 30–50 μm in size are seen interspersed throughout the anode matrix of Cell-2. Fig. 7 shows the EDS (energy dispersive spectra) spectrum of one such agglomerated particle. The in-set in Fig. 7 shows the spot on the agglomerate that was analyzed. The peak positions with binding energy for Y and Zr can be seen at 1.92 and 2.04 eV, respectively. No peak for Ni is seen, confirming the agglomerates to be YSZ particles. Fig. 8 shows the top view of the printed electrolyte. This micrograph corresponds to a region of the electrolyte in the vicinity

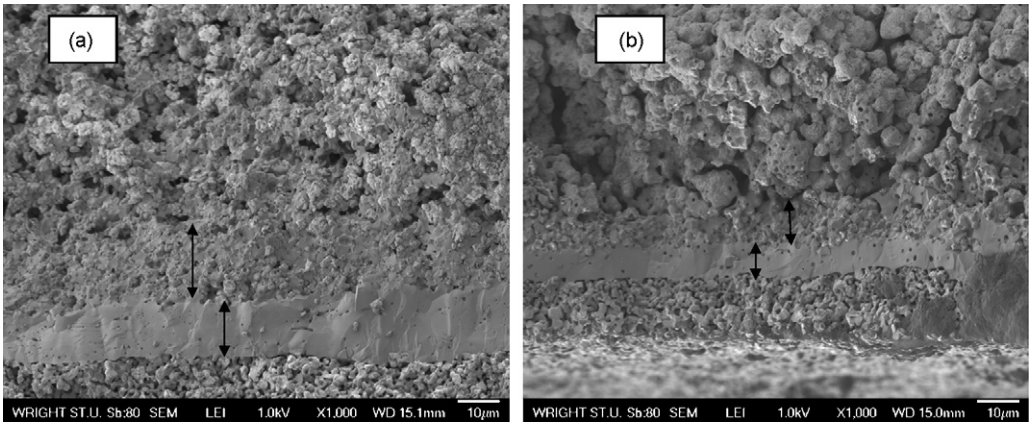

Fig. 5. Fracture cross-sectional scanning electron micrograph after electrochemical testing of (a) Cell-1 and (b) Cell-2 at a magnification of 1000×.

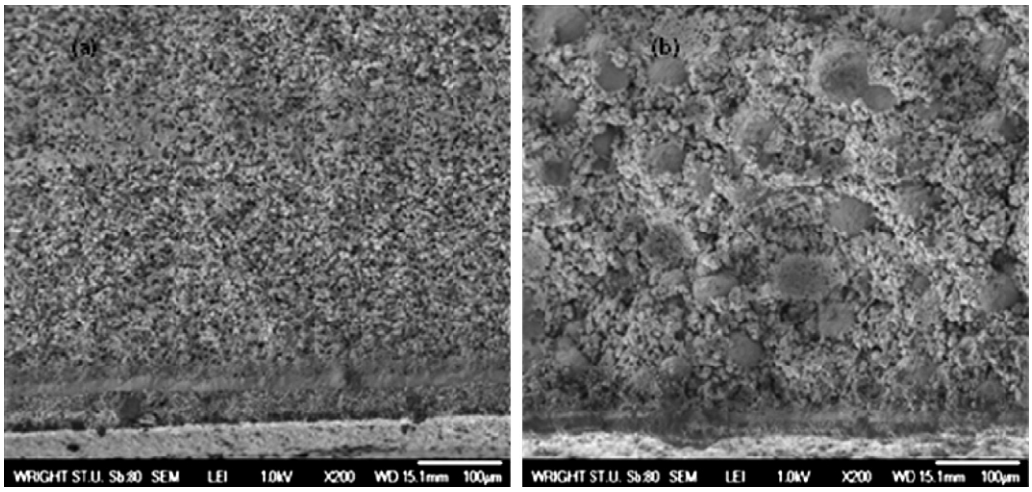

Fig. 6. Fracture cross-sectional scanning electron micrograph after electrochemical testing of (a) Cell-1 and (b) Cell-2 at a magnification of 200×.

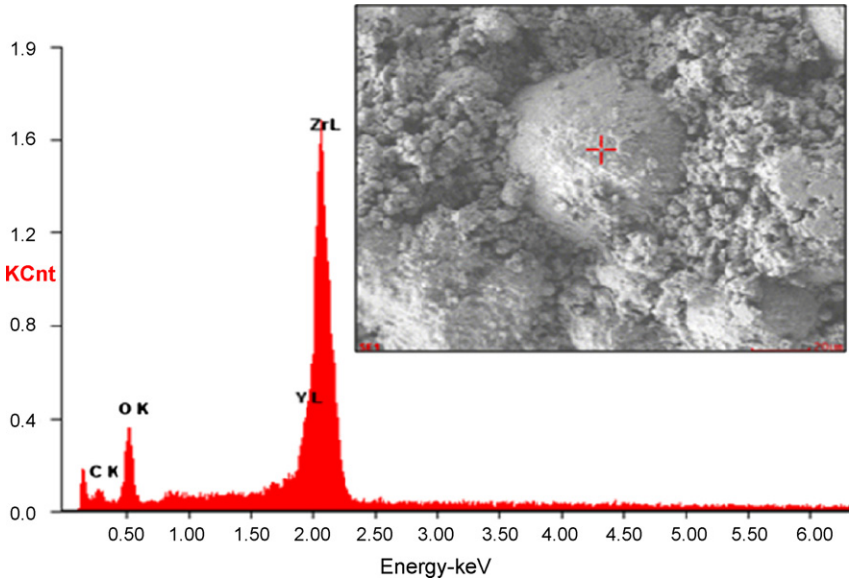

Fig. 7. EDS (energy dispersive X-ray spectra) of agglomerates in the anode of Cell-2; in-set is the agglomerate analyzed.

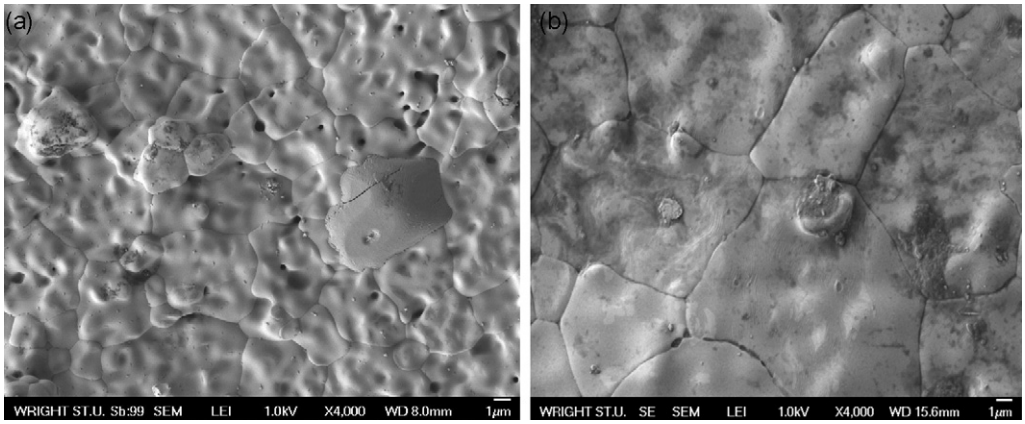

Fig. 8. Top view of the printed electrolyte of (a) Cell-1 and (b) Cell-2 used for electrochemical testing (this region is in the cathode side and corresponds to the area not covered by the cathode).

of the cathode of the tested cells. Well-formed grains of YSZ can be seen for both cells. The grains of YSZ of Cell-1 are seen to be smaller compared to that of Cell-2.

3.4. Correlation between microstructure, cell impedance and current characteristics

Qualitative assessment of cell microstructure as discussed in the previous section points to one clear difference between the two cells, besides a difference in the thicknesses of the electrolyte and interlayer, which relates to the anode. The differences between the two cells are given in Table 2. The difference in thickness of the printed layers of the two cells, while in part may be due to the differences listed in Table 2, these factors cannot account for almost twice the thickness of Cell-1 compared to Cell-2. Problems associated during printing such as clogging of jet head could have additionally contributed to a difference in wet thickness. The difference in grain size of the printed electrolyte, YSZ in the two cells is due, both to the difference in sintering temperature as well as the surface energy and roughness of the anode support. Both cells show a very tight anode interlayer-electrolyte interface compared to the anode-anode interlayer interface. There are no signs of delamination at any of these interfaces. While this observation corroborates the conclusion from impedance results with respect to absence of delamination, the qualitative microstructural observations are not sufficient to explain the increase in high frequency impedance in Fig. 2 that implies an increase in ohmic resistance or the deteriorating cell performance for temperatures >700 °C for Cell-1. Quantitative information about porosity, tortuosity and contiguity is required to better understand the behavior of the cells. For the case of Cell-2, reduced ohmic losses due to smaller thickness of electrolyte could lead to higher current density. However, this factor is insufficient to explain the improved stability at 750 °C as well the much higher current density. Moreover, the temperature variation of current density as well as cell impedances (relative variation of ohmic, R_Ω vs. non-ohmic resistances, R_p) are different for the two cells. The instability at 800 °C for Cell-2 is perhaps related to the inhomogeneous microstructure resulting from the difference in particle size of NiO and YSZ. Clearly, the overall microstructure (interfaces and bulk) determined by the precursor materials and method of processing impact the cell stability and performance. While this study is insufficient to isolate the impact of each of the parameter involved, it nevertheless points to the potential for further enhancement of printed cell characteristics by optimizing the several variables considered in this study and the need for a systematic variation of the various parameters that impact the microstructure and hence the performance of the cell.

4. Conclusions

In this work, ink-jet printing has been successfully used to fabricate the electrolyte and anode functional layers of a solid oxide fuel cell. Microstructural characterization reveals that ink-jet printing can be used to fabricate SOFC materials with the microstructures and layer morphology necessary for SOFC operation. The ink-jetted electrolyte layers examined in this paper are found to be largely or completely free of pinholes, and relatively thin in comparison to those electrolytes produced by more conventional ceramics processing methods. There is no evidence that this paper demonstrates the minimum electrolyte thickness possible by ink-jet printing. The authors of this paper expect that future ink-jet printing work might even demonstrate the successful fabrication of large-area electrolyte layers with thicknesses approaching submicron dimensions. Electrochemical characterization indicates a stable open circuit voltage, and the *I–V* data of these cells mandate further optimization of the microstructure to improve cell performance and stability. The comparison of the two cells in this work illustrates the use of ink-jet printing in the ongoing optimization of an SOFC structure. A more comprehensive effort is currently underway to systematically vary particle sizes of solids in the inks, and the thermal processing parameters needed to optimize the anode interlayers, anode and electrolyte.

In regards to future application of ink-jetting to SOFCs, the successful printing of the anode-interlayer is particularly significant. This result can be interpreted to suggest that ink-jetting is generally applicable to the fabrication of composite ceramic microstructures that contain significant porosity. Taken together, the data presented here strongly suggests that that ink-jetting could be used to produce all anode, electrolyte and cathode structures in a solid oxide fuel cell.

Acknowledgements

The authors wish to acknowledge the substantial contributions of Mr. Thomas Jenkins in materials processing and cell fabrication. Dr. Allen Jackson and Mr. Ian Barney are acknowledged for their assistance with the microscopy reported in this paper.

References

[1] N.Q. Minh, J. Am. Ceram. Soc. 76 (3) (1993) 563–588.
[2] S. Singhal, Solid State Ionics 135 (1–4) (2000) 305–313.
[3] S. Zha, P. Tsang, Z. Cheng, M. Liu, J. Solid State Chem. 178 (2005) 1844–1850.
[4] J. Serra, V. Vert, M. Betz, V. Haanappel, W. Meulenberg, F. Tietz, J. Electrochem. Soc. 155 (2) (2008) B207–B214.
[5] H. Yokokawa, N. Sakai, T. Horita, K. Yamaji, M.E. Brito, MRS Bull. 30 (8) (2005) 591–595.
[6] N. Sakai, H. Kishimoto, K. Yamaji, T. Horita, M.E. Brito, H. Yokokawa, J. Electrochem. Soc. 154 (12) (2007) B1331–B1337.
[7] T.L. Reitz, H. Xiao, J. Power Sources 161 (2006) 437–443.
[8] W. Bujalski, C.A. Dikwal, K. Kendall, J. Power Sources 171 (1) (2007) 96–100.
[9] B.T. Lee, A.H.M.E. Rahman, J.H. Kim, J. Am. Ceram. Soc. 90 (6) (2007) 1921–1925.
[10] T. Hibino, A. Hashimoto, T. Inoue, J. Tokuno, S. Yoshida, M. Sano, Science 288 (5473) (2003) 2031–2033.
[11] S.P. Simmer, M.D. Anderson, G.G. Xia, Z. Yang, L.R. Pederson, J.W. Sevenson, J. Electrochem. Soc. 152 (4) (2005) A740–A745.
[12] F. Teitz, H.P. Buchkremer, D. Stover, Solid State Ionics 152/153 (2002) 373–381.
[13] S.C. Singhal, K. Kendall (Eds.), High-temperature Solid Oxide Fuel Cells: Fundamentals, Design and Applications, Elsevier, UK, 2003.
[14] R. Vaben, D. Hathiramani, J. Mertens, V.A.C. Haanappel, I.C. Vinke, Surf. Coat. Technol. 202 (2007) 499–508.
[15] T. Franco, Z. Hoshiardin, P. Szabo, M. Lang, G. Schiller, J. Fuel Cell Sci. Technol. 4 (4) (2007) 406–412.
[16] L.R. Pederson, P. Singh, X.D. Zhou, Vacuum 80 (10) (2006) 1066–1083.
[17] M. Kuhn, T. Napporn, M. Meunier, S. Vengallatore, D. Therriault, J. Micromech. Eng. 18 (2008), 8 pp., 015005.
[18] R.C. Pullar, Y. Zhang, L.F. Chen, S.F. Yang, J.R.G. Evans, P.K. Petrov, A.N. Salak, D.A. Kiselev, A.L. Kholkin, V.M. Fereira, N.M. Alford, J. Eur. Ceram. Soc. 27 (16) (2007) 4437–4443.
[19] T.M. Wang, B. Derby, J. Am. Ceram. Soc. 88 (8) (2005) 2053–2058.
[20] X. Zhao, J.R.G. Evans, M.J. Edirisinghe, J.H. Song, J. Mater. Sci. 37 (10) (2002) 1987–1992.
[21] C. Ainsley, N. Reis, B. Derby, J. Mater. Sci. 37 (15) (2002) 3155–3161.
[22] A.D. Taylor, E.Y. Kim, V.P. Humes, J. Kizuka, L.T. Thompson, J. Power Sources 171 (2007) 101–106.
[23] A.V. Shevchenko, E.V. Dudnik, A.K. Ruban, Z.A. Zaitseva, L.M. Lopato, Powder Metall. Ceram. 42 (3/4) (2003) 145–153.
[24] B. Boukamp, Solid State Ionics 18/19 (1986) 136–140.
[25] V. Sonn, A. Leonide, E. Ivers-Tiffee, ECS Trans. 7 (1) (2007) 1363–1372.